PLANETARY SCIENCE

What makes low-frequency earthquakes low frequency

Qing-Yu Wang¹*, William B. Frank¹, Rachel E. Abercrombie^{1,2}, Kazushige Obara³, Aitaro Kato³

Low-frequency earthquakes, atypical seismic events distinct from regular earthquakes, occur downdip of the seismogenic megathrust where an aseismic rheology dominates the subduction plate boundary. Well situated to provide clues on the slip regime of this unique faulting environment, their distinctive waveforms reflect either an unusual rupture process or unusually strong attenuation in their source zone. We take advantage of the unique geometry of seismicity in the Nankai Trough to isolate the spectral signature of low-frequency earthquakes after correcting for empirically derived attenuation. We observe that low-frequency earthquake spectra are consistent with the classical earthquake model, yet their rupture duration and stress drop are orders of magnitude different from ordinary earthquakes. We conclude their low-frequency nature primarily results from an atypical seismic rupture process rather than near-source attenuation.



INTRODUCTION

Tiny repetitive earthquakes with a characteristic deficit of high-frequency seismic radiation called low-frequency earthquakes occur in swarms of activity at plate boundaries around the world. While they occur along many plate boundaries, low-frequency earthquakes most often occur in subduction zones (1) in the transition zone on the plate interface between major earthquakes and deeper steady creep. Their spatial distribution and distinct periodicity provide important insights into the nature of slip in this transitional region (2) and its relationship to large destructive earthquakes (3, 4), but the underlying cause of their distinctive seismic signature remains enigmatic.

The low-frequency nature of these events could reflect a novel seismic source, with abnormally slow rupture and slip velocities compared to regular earthquakes (5, 6), which are well explained by the classical ω -square circular rupture model (7), or they could be regular earthquakes with their high-frequency radiation attenuated away during propagation through the unusual source region in which they occur (8). Alternatively, some combination of the two is possible, as the unusual conditions needed to produce one are also likely to affect the other.

Regional three-dimensional (3D) imaging of seismic velocity (9, 10) and attenuation (11) structures provides a general context for the complexity of the plate boundary faulting system. Much research has highlighted the presence of high fluid content within the subduction interface zone (12), causing high fluid pore pressure (13, 14) and strong attenuation (15, 16). Regional studies over hundreds of kilometers cannot, however, constrain the narrow low-frequency earthquake source region at the plate interface.

A powerful approach to precisely isolating the spectral signature of an earthquake source is to use the recording of a colocated smaller earthquake as an empirical Green's function to remove the waveform distortion due to propagation along the path from the source region to the recording seismometer (17). The low signal-to-noise and small size of low-frequency earthquakes prevent this approach from being applied directly. Thomas *et al.*

(18) used nearby shallower earthquakes as empirical Green's functions to resolve the source characteristics of low-frequency earthquakes on the San Andreas fault. However, if the recorded deficit of high frequencies was a consequence of localized attenuation in the source zone, then this approach is unable to distinguish whether the attenuation between the low-frequency earthquakes and the shallower empirical Green's functions is responsible for the characteristic spectral shape of low-frequency earthquakes. Similarly, the low seismicity rates on the Cascadia subduction zone forced Bostock et al. (15) to use earthquakes over a 100 km region as empirical Green's functions to investigate the source characteristics of low-frequency earthquakes on the plate interface at depth. Resolving this outstanding question requires a combined analysis of both earthquakes and low-frequency earthquakes in a region where many of each type of seismic event occurs in an optimal geometry to isolate source and path effects.

The Nankai Trough, where low-frequency earthquakes were first observed (19), is monitored by a long-term borehole monitoring network (20) that has recorded low-frequency earthquakes in the same epicentral area as both crustal and intraslab earthquakes (Fig. 1). We focus on two depth columns directly beneath two seismic stations where the subduction interface is sandwiched between earthquakes above and below, with one depth column hosting low-frequency earthquakes and the other not. With this unique seismic geometry, we investigate the end-member possibilities of attenuation experienced by low-frequency earthquakes to isolate their source process. Through this natural controlled experiment, we place key constraints on the character of the low-frequency earthquake source to address the outstanding question: What makes low-frequency earthquakes low frequency?

RESULTS

Experimental setup

We define two 10-km-radius-depth columns of seismicity beneath two Hi-net (high-sensitivity seismograph network) (20) borehole seismometer stations TOKH and TKWH (Fig. 1A), using the Japan Meteorological Agency (JMA) catalog of local earthquakes between 2005 and 2018. Low-frequency earthquakes only occur beneath TKWH (the orange column), located on Kii Peninsula, while none are observed beneath eastern Shikoku Island beneath

¹Department of Earth, Atmospheric and Planetary Sciences, Massachusetts Institute of Technology, Cambridge, MA, USA. ²Department of Earth and Environment, Boston University, Boston, MA, USA. ³Earthquake Research Institute, University of Tokyo, Bunkyo, Tokyo, Japan.

^{*}Corresponding author. Email: qingyuwa@mit.edu

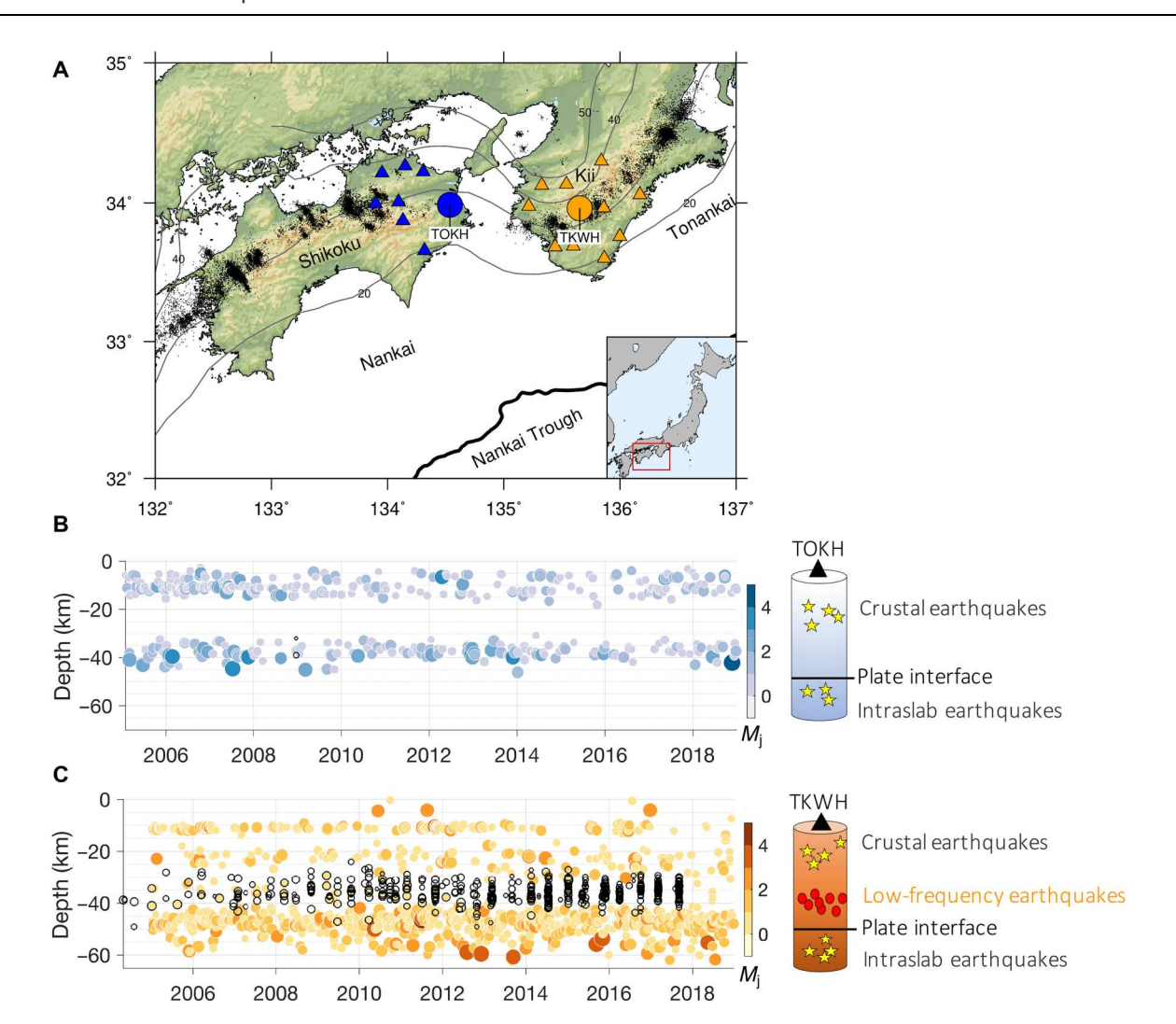


Fig. 1. Spatiotemporal behavior of low-frequency and regular earthquakes in the Nankai Trough. (A) Map view of two neighboring localized regions of seismicity with and without low-frequency earthquake activity. Black circles represent the low-frequency earthquakes from 2005 to 2018 as cataloged by the JMA. We focus on depth columns beneath two seismic stations, TOKH in blue where no low-frequency earthquakes occur and TKWH in orange where low-frequency earthquakes do occur; other analyzed neighboring stations are shown by the colored triangles. The black thin lines indicate the plate boundary of the Philippine Sea slab (*54*), and the black thick line illustrates the Nankai Trough, where the Philippine Sea Plate is subducting beneath southwestern Japan. (**B** and **C**) Depth distributions of regular earthquakes and low-frequency earthquakes (black circles) within the two 10-km-radius-depth cylinders beneath TOKH and TKWH; low-frequency earthquakes only occur beneath the orange depth cylinder (TKWH).

TOKH (the blue column), a real gap in low-frequency earthquake activity verified by a recent joint analysis with permanent and temporary observations (21). The local magnitudes M_j for regular earthquakes estimated from peak seismic velocities range from 0 to 4.1; low-frequency earthquake with magnitudes larger than magnitude (M_j) 1 are not observed. We observe regular earthquakes in the overriding plate crust and just below the subduction interface within the downgoing oceanic slab throughout the studied time period in both depth columns (Fig. 1, B and C). Within the orange column, low-frequency earthquakes occur in discrete bursts of activity (22) at \sim 30 to 40 km in depth, consistent with the depth of the plate interface (6, 23, 24). The apparent vertical extent of the low-frequency earthquake source region is likely overestimated because of significant location errors in depth due to a lack of observable P-wave arrivals (Fig. 1) (19).

We start by relocating the regular earthquakes from their original JMA catalog locations, using a double-difference travel time approach that leverages interevent waveform correlation (25). This approach explicitly groups the earthquakes into clusters defined by both their spatial proximity, defined by the double-difference travel times, and their similarity in source mechanism, defined by their interevent waveform correlations. This explains why there are distinct clusters shown in fig. S1 that are tightly grouped together in space: Their waveforms, and thus their source mechanisms, distinguish a given cluster from the other nearby clusters. We use this organization of the catalog into clusters to first evaluate the seismic structure of the two depth columns and then to constrain the spectral shape of low-frequency earthquakes.

Vertical structure along the low-frequency earthquake path

A precise local seismic structure is essential context to accurately capture the faulting environment of the low-frequency earthquake source region. We constrain the vertical profile of seismic velocity and attenuation within both depth columns at high resolution using all of the relocated regular earthquakes (fig. S3B). We use the manually picked *P*- and *S*-wave arrival times to invert for the velocity structure of both *P* and *S* waves (Fig. 2, A and B), initialized with a regional a priori seismic velocity model (9).

In the blue column, both the P and S seismic velocity profiles have a comparable shape to the initial model, increasing steadily with depth except close to the plate interface where they exhibit a rapid change. The sharp velocity contrast expected at the interface is difficult to recover because the earthquake location errors are probably larger than the depth range of the velocity changes. In contrast, the P and S velocities in the orange column exhibit significant variation with depth and deviation from the initial model. Both velocities decrease below \sim 20 km and remain low throughout the low-

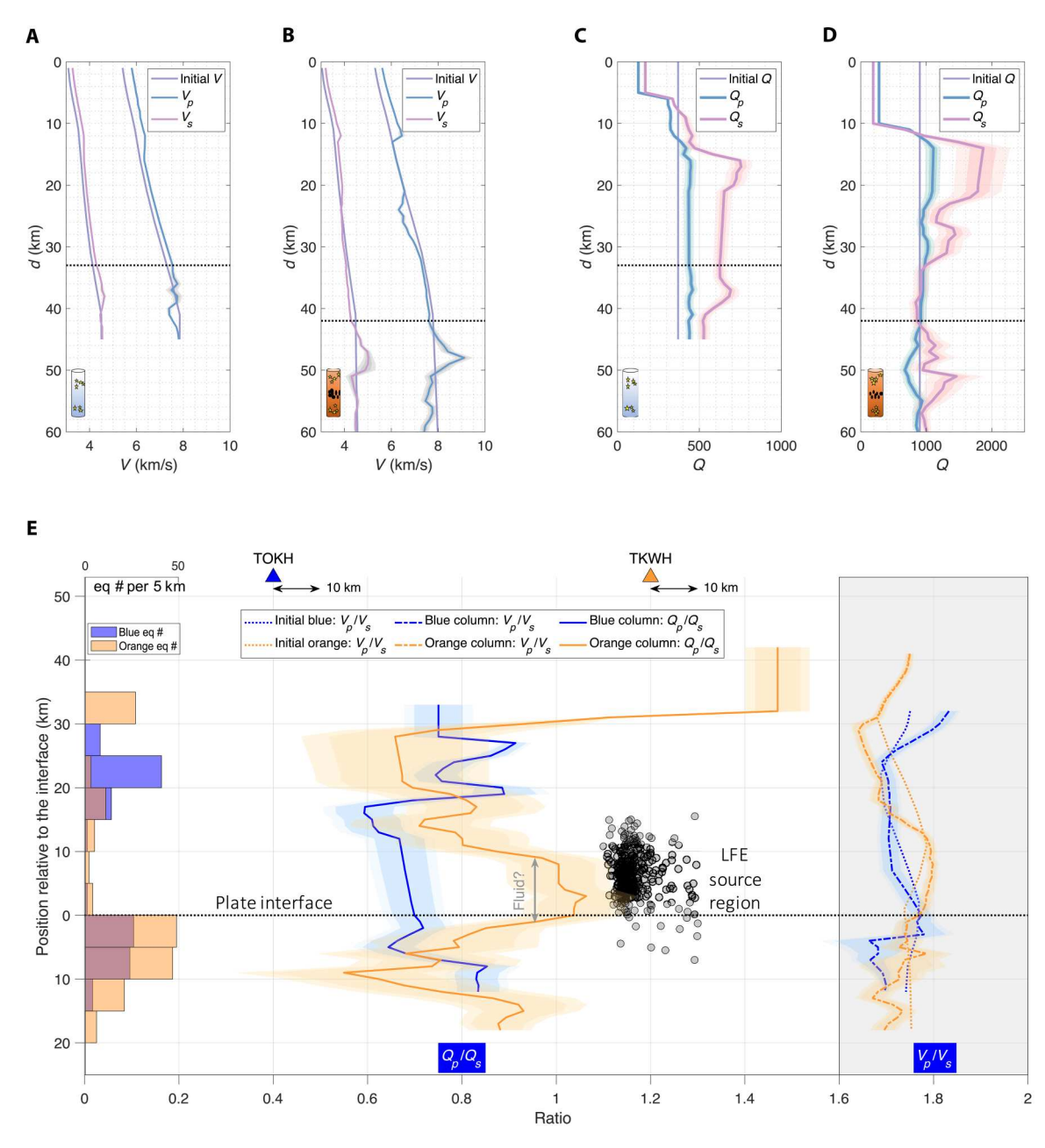


Fig. 2. Seismic velocity and attenuation structure of the two depth columns. (A and B) respectively show the 1D velocity structure within the blue and orange columns. (C and D) respectively show the 1D seismic Q structure within the blue and orange columns. The black dotted lines indicate the shallowest depth of intraslab earthquakes, assumed to be the slab interface for the purpose of aligning the two columns in (E). The shaded zones outline the uncertainty estimated as two times the SD. (E) Ratios of V_p/V_s (dotted blue and orange curves) and Q_p/Q_s (solid blue and orange curves) within the blue and orange columns. The black dots indicate the low-frequency earthquakes scaled by longitude within the orange column. The colored bars indicate the number of earthquakes in 5-km-depth bins within the two columns.

frequency earthquake source region (26, 27). At the depth of the plate interface, they increase rapidly, similar to the behavior in the blue column. We observe a high V_p/V_s ratio within the low-frequency earthquake source region that is not present elsewhere, consistent with increased fluid pressure where low-frequency earthquakes occur (23). We also use a joint inversion (28) to simultaneously invert the absolute earthquake hypocenter and the 1D seismic velocity structure, using all adjacent seismic stations. The results of the joint inversion confirm the reliability of our seismic velocity model and corroborate the high V_p/V_s ratio within the low-frequency earthquake source region (fig. S6).

To determine the attenuation structure, we first estimate the local site effects beneath each station and then invert for the path-averaged attenuation. Using our high-resolution seismic velocity profile in Fig. 2 (A and B), we recover the local attenuation structure with depth (Fig. 2, C and D). Given the uneven depth distribution of earthquakes (Fig. 2), we invert for a constant quality factor Q within the first 5 and 10 km for the blue and orange columns, respectively. Both profiles are comparable to the seismic attenuation structure estimated by Kita and Matsubara (11), but our results reveal more detail in depth, especially in the orange column, which displays a high Q zone at a relatively shallow depth of \sim 10 to 20 km, possibly associated with the Kumano pluton (29), that decreases with depth and then increases beneath the interface.

To evaluate our horizontal spatial resolution of the structure within the 10-km radius of the depth columns, we estimate the Fresnel zones of the earthquake clusters as they travel through the low-frequency earthquake source region. We observe in fig. S2C that any given cluster of earthquakes, each well constrained by their differential travel times and waveform correlations, is more widely distributed than their respective Fresnel zones. This suggests that the epicentral location errors are greater than the Fresnel zones, implying that our recovered seismic structure likely represents an areal average across the entire 10-km-radius-depth column.

We then focus on the ratios of Q_p/Q_s and V_p/V_s that are both indicators of the presence of pore fluids (30). We plot together these ratios in both depth columns after removing a reference depth from the shallowest intraslab earthquake (Fig. 2E), which we consider to be the deepest possible extent of the subduction plate interface. This relative reference frame enables us to directly compare the seismic structure of the two depth columns. For both V_p/V_s and Q_p/Q_s , the shallowest ~10 km is strongly affected by shallow heterogeneity and poorly resolved in our models (fig. S3A). At greater depths the V_p/V_s ratio is similar to previous observations in Japan (31, 32). Overall, the Q_p/Q_s in both columns is less than 1. It is only in the orange column, within the 10 to 15 km above the plate interface reference depth, that the Q_p/Q_s ratio approaches unity; this coincides with a V_p/V_s significantly greater than the crustal reference value of 1.74 (33). This region of high V_p/V_s and Q_p/Q_s in the orange column just above the plate interface suggests pore space saturated with fluids (30), likely originating from metamorphic dehydration reactions (16, 32). The high V_p/V_s and Q_p/Q_s in the orange column both decrease upward from the plate interface reaching average values about 15 km above the plate interface, coinciding with a high absolute Q_s . This suggests an impermeable barrier above the Philippine Sea Plate near or at the base of the upper plate that maintains a high pore fluid pressure, likely a key ingredient in generating low-frequency earthquakes (23). We suggest that this observed seismic structure of the orange column

indicates a fluid-rich environment within the low-frequency earthquake source region (34) above the plate interface, likely facilitating seismic rupture by reducing the effective normal stress. With no evidence of a singular zone of attenuation responsible for the unique spectral content of low-frequency earthquakes, we now turn to the seismic waveforms of low-frequency earthquakes to constrain their source signature.

Earthquake-like spectral shape of low-frequency earthquakes

The displacement spectra of regular earthquakes in both depth columns exhibit typical magnitude-dependent scaling of their spectral shape, with larger low-frequency amplitudes and lower corner frequencies with increasing magnitude (Fig. 3). The spectra of low-frequency earthquakes in the orange column are visible over the noise with their eponymous deficiency in high frequencies when compared to regular earthquakes.

Leveraging the waveform similarity defined by our relocation approach, we use earthquake clusters to extract local empirical attenuation functions shown in Fig. 3C that include path effects that cannot be explained by simple exponential attenuation models (see Materials and Methods for details). We constrain the empirical attenuation separately for each earthquake cluster, allowing us to precisely estimate the attenuation at different depths, notably surrounding the low-frequency earthquake source region. We once again observe a layer with relatively low attenuation (high-quality factor Q) at \sim 20 km in depth, above the low-frequency earthquake source region (Fig. 2D). Consistent with the uncorrected displacement spectra of regular earthquakes in Fig. 3 and the resolved seismic structure of attenuation, the recovered empirical attenuation does not show evidence of a localized, strongly attenuating region in the orange column that would explain the observed deficiency of high-frequency energy in low-frequency earthquake spectra.

We average the empirical attenuation functions across three earthquake clusters at ${\sim}45$ km, the deep extent of the low-frequency earthquake source region, to isolate the spectral signature of the low-frequency earthquake source; this average represents the maximum attenuation that low-frequency earthquakes could experience. We divide this average empirical attenuation function from the averaged displacement spectra of low-frequency earthquakes separated into two magnitude bins, 0.2 to 0.5 and 0.5 to 1. We observe in Fig. 3D that the rate of high-frequency decay of low-frequency earthquakes after correction now matches an ω -square falloff, suggestive of an earthquake-like circular rupture.

We observe a subtle magnitude-dependent scaling of the corner frequency f_c of low-frequency earthquakes (Fig. 3D), consistent with regular earthquakes (Fig. 3, A and B). Noise at frequencies lower than 2 Hz precludes us from determining a corner frequency for the largest low-frequency earthquakes, but the maximum possible corner frequency f_c of the low-frequency earthquakes observed here is about ~2 to 3 Hz (35). A corner frequency of 3 Hz is more typical for a magnitude 4 earthquake, three magnitude units greater than the largest low-frequency events observed here, indicating how anomalous these events are. The representative stress drop estimated from this maximum possible corner frequency is ~10 kPa, about two orders of magnitude smaller than that of regular earthquakes. If we assume a source dimension of 50 m, the rupture radius more typical of an earthquake of similar moment

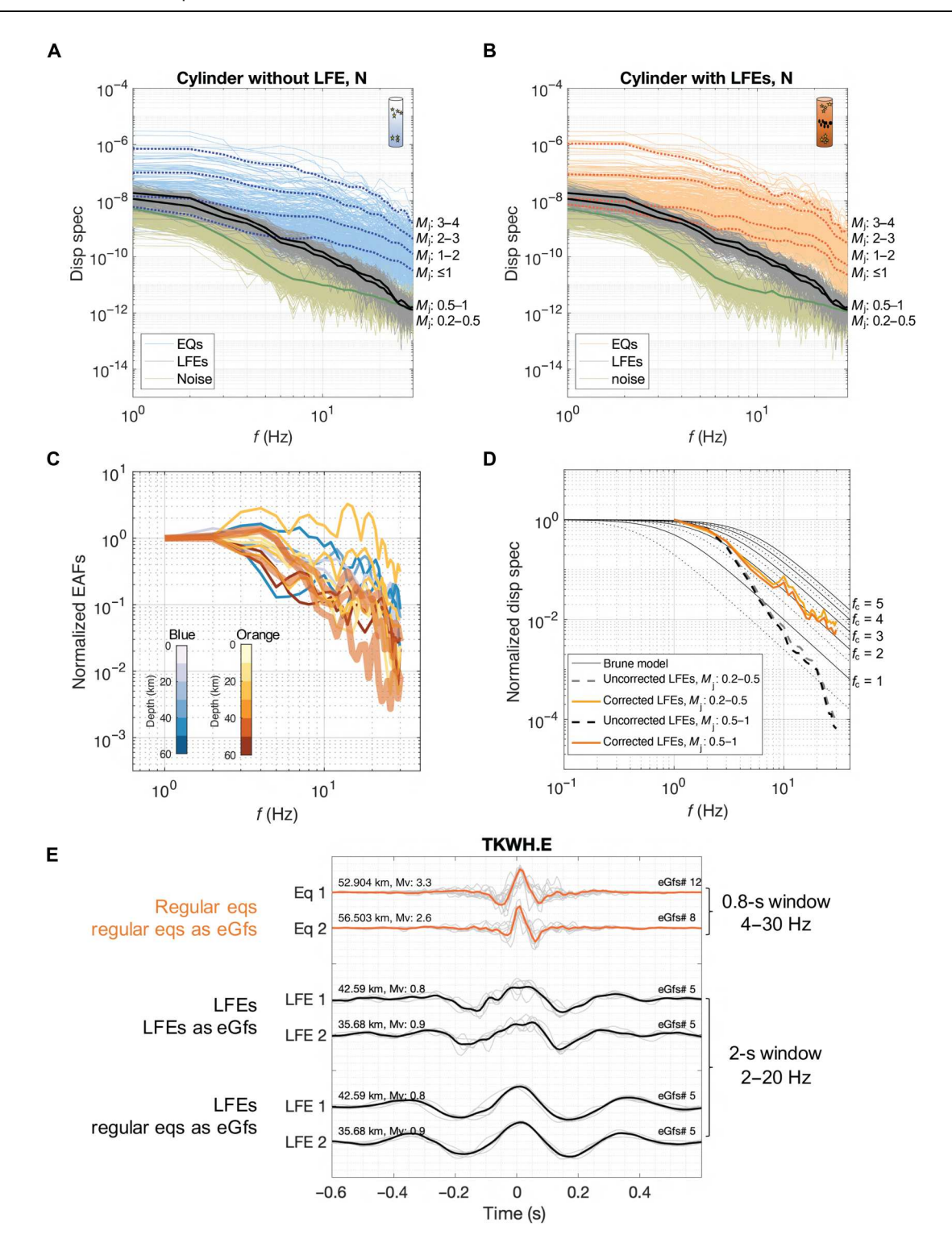


Fig. 3. Distinct spectral signatures of low-frequency and regular earthquakes in the Nankai Trough. (A and B) are S-wave displacement spectra of regular earthquakes and noise within blue and orange depth columns, respectively. The gray curves are S-wave spectra of low-frequency earthquakes from only the orange depth column. Thick black and green lines are averaged spectra of low-frequency earthquakes and noise, respectively. (C) The empirical attenuation functions (EAFs) are retrieved from regular earthquakes from both blue and orange depth columns. (D) Normalized spectra of larger (dashed, black) and smaller (dashed, gray) low-frequency earthquakes before and after correction with empirical attenuation functions (bold lines) shown in (C). Black lines show ω-square models with example corner frequencies f_c . (E) Example source-time functions for both regular earthquakes and low-frequency earthquakes after deconvolving S-wave empirical Green's functions (eGfs).

magnitude (Fig. 3), then the rupture velocity would have to be 100 m/s for a source duration of 0.5 s ($1/f_c$ = 2 Hz), more than one order of magnitude smaller than typical earthquake rupture velocities.

We evaluate how robust our source estimates of low-frequency earthquakes are by examining their source-time functions in the time domain, the result of a reverse Fourier transform of their displacement spectra corrected with an empirical Green's function. We estimate source-time functions for the largest low-frequency earthquakes (Fig. 3E) with estimated magnitudes of 1 with two different sets of empirical Green's functions, one using regular earthquakes similar to (18) and one with smaller low-frequency earthquakes. The source-time functions of low-frequency earthquakes show simple earthquake-like pulses, albeit with a much longer duration than even a regular earthquake of magnitude $M_{\rm j}=3.3$. We verify the resolution of our source-time functions with regular earthquakes and observe simple pulse shapes with an expected slightly longer duration for larger magnitude events (Fig. 3E and fig. S7D).

Assuming that rays from deep earthquakes pass through the region where low-frequency events occur in the orange column, the observed difference in spectra between regular earthquakes and low-frequency earthquakes cannot be explained by the greatest possible attenuation below the subduction interface where low-frequency earthquakes occur, as estimated from intraslab earthquakes. This contrasts with recent experimental work on lithologies suspected to host low-frequency earthquakes (36). Our results indicate that the absence of high-frequency components in low-frequency seismic events is not primarily controlled by abnormally high attenuation. As discussed above, epicentral location errors and the wide distribution of estimated Fresnel zones suggest that our empirical estimates of attenuation, while horizontally averaged over the depth column (fig. S2B), accurately represent the impact of the source-receiver path on the recorded low-frequency earthquake waveforms. In addition, the similarity of low-frequency earthquake source-time functions, whether computed with regular earthquakes or low-frequency earthquakes, suggests that strong lateral heterogeneity is unlikely to explain our results. We thus conclude that attenuation is not solely responsible for the distinctive spectral signature of low-frequency earthquakes and that the low-frequency earthquake source is significantly different from the typical earthquake source. We suggest that this distinct faulting source is likely influenced by the unique faulting environment that hosts low-frequency earthquakes: the fluid-rich subducting plate boundary.

DISCUSSION

Our findings indicate that distinct structural factors dictate the occurrence and characteristics of low-frequency earthquakes. After correcting with precise empirical attenuation functions, we observe that low-frequency earthquakes are consistent with the ω -square high-frequency spectral falloff and the simple pulse of source-time function that explains the majority of earthquake sources (7). This indicates a similar rupture process for regular and low-frequency earthquakes that can be modeled as a circular crack. As the slip velocity on the fault controls high-frequency seismic radiation (7), high frequencies are preferentially generated by abrupt changes in rupture velocity. The presence of fluids, supported here by our local estimates of 1D seismic velocity and attenuation, can not only affect the dynamic rupture propagation by reducing dynamic friction (37) but also slow down rupture speeds

through dilatancy strengthening (38). Compared to dry conditions, fluids can cause frequency-dependent attenuation to dominate under saturated conditions (36) that is difficult to model. We side-step this challenge by correcting low-frequency earthquake spectra with empirical estimates of attenuation that do not rely on a given model (Fig. 3). By comparing two neighboring depth columns, we demonstrate that attenuation with a lateral resolution of 20 km contributes to, but cannot alone explain, the unique spectral signature of low-frequency earthquakes (Fig. 2).

We demonstrate at a higher resolution than past regional-scale studies (11, 23) that the local environment of the plate interface is different in areas where low-frequency earthquakes occur compared to nearby areas where they do not. The source regions of the lowfrequency earthquakes are marked by high pore fluid pressure indicated by high Q_p/Q_s and V_p/V_s ratios (Fig. 4). This suggests that local variations in the rheology of this transitional zone, just downdip of where major earthquakes occur and where slow fault slip dominates the tectonic slip budget, are responsible for earthquakes that rupture an order of magnitude more slowly than is typical. Metamorphic dehydration of the downgoing oceanic crust likely facilitates this slip regime by increasing pore fluid pressure and creating the necessary stress conditions to host seismicity. An atypical rupture mechanism associated with this rheology, likely governed by processes linked to saturated fault conditions at the plate boundary, is necessary to explain the source of low-frequency earthquakes. The unique rheology of low-frequency earthquakes has implications for the potential occurrence of transient slow slip events, which can impact the interseismic loading of the megathrust. Observation of low-frequency earthquakes suggests that the fault system is likely accumulating strain that will not be released in a major earthquake but rather as an aseismic slow slip event. Further work will be essential to explore the physical mechanisms that can explain the rupture dynamics observed here, shedding light on the role the transitional zone downdip of the seismogenic megathrust plays in the seismic cycle.

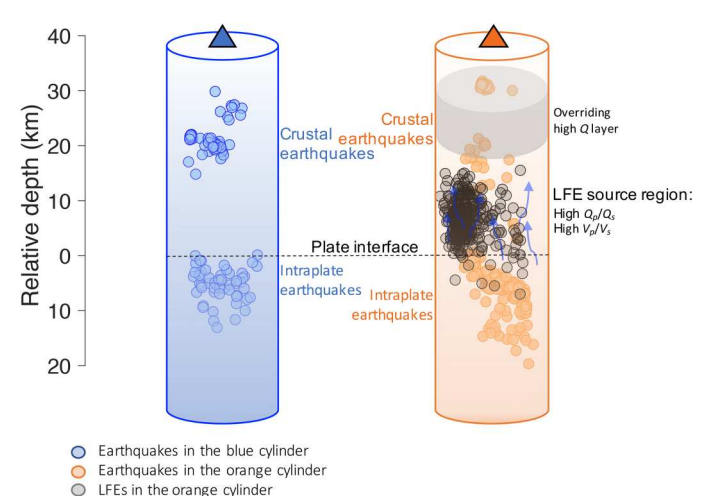


Fig. 4. Schematic attenuation structure in both analyzed depth columns. Blue and orange points are regular earthquakes used for the structural inversion. Black points represent low-frequency earthquakes, which only occur in the orange column. Triangles represent the two seismic stations that are centered in each respective depth column.

MATERIALS AND METHODS

Earthquake relocation and clustering

We relocate all the regular earthquakes in two columns with a 10km radius centered on Hi-net seismic stations TOKH and TKWH (Fig. 1). We use seismic recordings from all the available Hi-net stations close enough to record the small earthquakes: 8 for the blue column of earthquakes and 11 for the orange column. Our relocation, done separately for each depth column, is based on the Grow-Clust relocation approach (25), which uses double-difference travel times and waveform correlation. We only attempt to relocate events with magnitudes (M_i) larger than 0.5 and 0.8 for the blue and orange groups, respectively. The magnitude criteria are designed to ensure sufficient signal-to-noise ratio for the P and S waves while maintaining the required number of earthquakes for the depth-dependent analysis. We only use the differential travel times to relocate if the corresponding correlation coefficient is greater than 0.7 (39) for both P and S waves at 4 to 8 Hz using a 1-s window length for a given event pair at one station.

Figure S1 (A and B) illustrates earthquake hypocenters in both depth columns before and after the earthquake relocation. Starting from the JMA catalog from 2005 to 2018, we are able to relocate 313 of 454 regular earthquakes in the blue column and 409 of 526 regular earthquakes in the orange column. The relocation produced negligible difference in epicenters, consistent with the known quality of the JMA catalog (40). In both column configurations, the earthquakes are concentrated within layers, including shallow crustal earthquakes and deep intraslab earthquakes.

The relocation (25) involves grouping the relocated events into distinct clusters by combining the hypocentral locations with the waveform similarity determined during cross-correlation. In fig. S1 (C and D), different colors are used to distinguish the relocated clusters containing at least 10 earthquakes. Although several earthquake clusters are located in the vicinity of other clusters at comparable depths, they are grouped into distinct clusters based on waveform cross-correlation constraints at multiple stations. We are thus able to control for earthquake mechanism by leveraging both locations and waveforms. The high correlation coefficient threshold we chose allows us to extract clusters of earthquakes with both similar focal mechanisms and locations. Earthquakes having a magnitude M_i greater than 2.5 are considered to be target earthquakes for studying the source features, attenuation characteristics, and stress changes within the localized depth columns.

Low-frequency earthquake locations and lateral heterogeneity

The locations of the low-frequency earthquakes from the JMA catalog are within the depth interval of ~30 to 40 km in the orange column (Fig. 1C). Without identifiable *P*-wave arrivals (19), the low-frequency earthquake epicentral locations are more robust than their poorly constrained depths. The overly broad range of depths of the low-frequency earthquakes corroborates that their locations in depth are much more uncertain (Fig. 1C). Our experimental setup to constrain attenuation in the low-frequency earthquake source region rests on the assumption that the 10-km-radius-depth columns are sufficiently small that the seismic waves radiated from all of the seismic events in the depth column experience the same seismic structure as they travel to the station

directly above. This assumes that all seismic waves traverse the low-frequency earthquake source region in the orange column. To evaluate the horizontal coverage of our recovered seismic structure, we estimate the Fresnel zone of the seismic waves traveling through the low-frequency earthquake source region. The Fresnel zones shown in fig. S2C represent the lateral coverage sampled by the seismic waves from the earthquakes at 4 Hz and their spatial relationship with the distribution of low-frequency earthquakes. Figure S2 (A and B) depicts the spatial distribution of the target earthquakes in the two depth columns.

We estimate the radius of the Fresnel zones (41) of the five intraslab earthquake clusters in the orange column using

$$r = \frac{v}{2} \sqrt{\frac{t_0}{f}} \tag{1}$$

where ν is the velocity from the local 1D profile and t_0 is the travel time between each individual earthquake epicenter and the median depth of low-frequency earthquakes of approximately 36 km; we calculate this travel time between each individual intraslab earthquake hypocenter and this median depth of 36 km. We observe that the Fresnel zones of the relocated earthquake clusters with significantly similar waveforms do not overlap as much as expected, suggesting that the epicentral location errors are greater than the Fresnel zones. The spatial distribution of these waveform-based earthquake clusters demonstrates that we cannot recover the lateral heterogeneity within the 10-km radius of each depth column. Our estimates of seismic velocity and attenuation thus likely represent the horizontally averaged attenuation across the depth column, which accurately accounts for the impact of the source-receiver path on the low-frequency earthquake waveforms recorded at the stations at the top of each depth column.

Seismic velocity structure

We jointly invert 1D P- and S-wave velocities down to 45 km beneath TOKH and 60 km beneath TKWH (Fig. 2, A and B) using the manually picked P- and S-wave arrival times t_p and t_s and hypocenter depths of all relocated events (fig. S3A). We adopt a least-squares inversion and reject earthquakes with incident angles of \geq 25° to avoid bias from shallow structure. We select a regional seismic velocity model (9) and extract a separate 1D velocity model for each depth column separately from the grid point closest to the two central stations. We then interpolate each model to every 1 km to form our two initial velocity models m_0 . We jointly invert the 1D velocity of both P and S waves using

$$m = (G^{\mathrm{T}}C_{\mathrm{D}}^{-1}G + C_{\mathrm{M}}^{-1})^{-1}(G^{\mathrm{T}}C_{\mathrm{D}}^{-1}d^{\mathrm{obs}} + C_{\mathrm{M}}^{-1}m_{0})$$
 (2)

by minimizing the least-squares misfit

$$\chi(m) = \frac{1}{2} \sum_{i=1}^{N} \frac{1}{\varepsilon_i^2} \left(d_i^{\text{obs}} - \sum_{j=1}^{n} G_{ij} m_j \right)^2 + \frac{1}{2} \sum_{i=1}^{n} \frac{1}{\gamma_i^2} (m_i - m_{0i})$$
 (3)

where $C_{\rm D}$ is identity matrix considering uniform input uncertainties ε and $C_{\rm M}$ is the diagonal matrix composed of squared γ . The larger γ is, the less dominant the initial model is. We select the final γ based on the inflection point from L curve of root mean square misfit $\chi^{\rm rms}$ against $|m_0-m|$ (fig. S3C).

We use a bootstrapping scheme to estimate uncertainties for the 1D inversions. We take a random 80% subset of the observations and the invert for the 1D structure; we perform this over 200 iterations. The root mean square residuals for the velocity inversion are reduced by 79 and 58% for the blue and orange columns, respectively. We then estimate the uncertainty as $1\times$ and $2\times$ the SD σ of these 200 iterations. The uncertainty for the velocity ratio (σ_R^2) is then determined by the following equation

$$\sigma_{\rm R}^2 = \left(\frac{\sigma_{V_p}}{\overline{V_p}}\right)^2 + \left(\frac{\sigma_{V_s}}{\overline{V_s}}\right)^2 \tag{4}$$

Joint-inversion of earthquake location and seismic velocity

To ensure the robustness of the resolved local seismic velocity structure and earthquake relocation, we also conduct a joint inversion of the local seismic velocity and earthquake hypocenters. (28). We use all the surrounding Hi-net stations, 9 and 11 stations in the blue and orange regions (Fig. 1A) respectively, and include all the earthquakes with both P- and S-wave arrival times from at least eight stations. We successfully locate 107 of 454 and 299 of 526 earthquakes respectively in the blue and orange depth columns.

Figure S4 depicts the earthquake locations in the blue and orange regions after 10 iterations, where each iteration allows for a 5 km fluctuation in earthquake depth. The final earthquake locations in both regions are comparable to the initial JMA locations and Grow-Clust results, with no significant differences observed.

Figure S5 illustrates a comparison between the velocity structures shown in Fig. 2 (depth resolution of 1 km) and the joint inversion that is designed to recover velocities with a 2-km-depth sampling. The root mean square residuals from the joint inversion remain in the range of 0.2 to 0.25 s, suggesting an error in depth of around 2 km.

The distribution of earthquakes within the blue depth column is suboptimal and does not provide significant local detail beyond the initial model. By using all of the surrounding Hi-net stations, the joint inversion produces an average velocity structure that covers an area of approximately 10,000 km ², which is not capable of accurately reflecting the complex structure within the studied depth columns. In addition, the shallow portion of the structure is mostly influenced by shallow ray paths reflecting the path to all of the surrounding stations. This shows that the local 1D velocity inversion, as well as the joint inversion of earthquake location and velocity structures, can both effectively resolve the important low S velocity zone, as indicated by the black arrow in fig. S5B.

The comparison of V_p/V_s obtained from the inversions using either a single station or the joint inversion of velocity and hypocenter indicates a noticeable high V_p/V_s zone within the depth range of low-frequency earthquakes source zone above the plate interface in the orange column (fig. S6).

Empirical Green's function and source-time functions of regular earthquakes

The empirical Green's function method uses small earthquakes in the vicinity of the main earthquake to cancel out the main event's path, site, and instrumental effects (42). Events to use as empirical Green's functions need to be carefully selected to ensure that they are smaller than the mainshock and share a similar focal mechanism and hypocenter with the mainshocks (42). We select empirical

Green's functions and target earthquakes from the earthquake clustering.

We only use seismogram pairs with a cross-correlation coefficient larger than 0.7 in the frequency range of 4 to 30 Hz for both P and S waves; across both depth columns and all target events, this criterion is met for between 4 and 11 stations per event pair. We correct for slightly different travel times by aligning the waveforms by cross-correlation. Figure S7A shows one example of a P-wave seismogram of a target earthquake and the nine empirical Green's functions in the same cluster (fig. S1, C and D). We estimate the corresponding spectra using the multitaper approach (43) for a 0.8-s time window for P waves and 1-s window for S waves. We then calculate the spectral ratios at each station to eliminate effects coming from the path and site and the trade-off between f_c and t^* (44). Figure S7B shows the spectral ratios obtained from each pair of target and empirical Green's function earthquakes in the frequency range of 2.5 to 30 Hz.

We isolate earthquake sources by averaging the normalized ratios of all pairs of target and empirical Green's function events for each target earthquake at each station. Figure S7C depicts an example of *P*-wave spectral ratios from the *Z* component for the 11 total target earthquakes at station TKEH in the orange station group. We only retain the ratios when the signal-to-noise ratio in the frequency range of 4 to 30 Hz for each earthquake pair is larger than 3. We obtain the spectral ratio for each target earthquake in either group that is well recorded by at least four stations. After deconvolution, we observe in fig. S7D clear and simple source-time functions for each of the target earthquakes, with large magnitude events with durations that increase with magnitude.

Probabilistic inversion of source properties

We perform an empirical Green's function analysis (42) to retrieve the corner frequency of each of the target earthquakes using the equation

$$R(f) = \frac{\Omega_{01}}{\Omega_{02}} \frac{\left[1 + \left(\frac{f}{f_{c2}}^{n_2 \gamma_2}\right)\right]^{1/\gamma_2}}{\left[1 + \left(\frac{f}{f_{c1}}^{n_1 \gamma_1}\right)\right]^{1/\gamma_1}}$$
(5)

Assuming that $\gamma = 2$ and n = 2, we then invert for the displacement source spectra of the target events at all of the surrounding stations, imposing a single f_c per event across the network. Instead of directly obtaining the apparent best result for each fitted parameter, we estimate the probability distribution of model parameters to propagate the likelihood (fig. S8). We adopt a Bayesian inference to derive the posterior probability from our inversion of f_c for each target earthquake (45)

$$\Phi(m) = \sum_{i}^{i=N} w(i) [g(m) - R_{\text{obs}}]^{T} C_{e}^{-1} [g(m) - R_{\text{obs}}]$$
 (6)

where N is the total number of stations, ranging from 4 to 11 for the target earthquakes across both depth columns, and $\Phi(m)$ is defined as the misfit between observation of ratios $R_{\rm obs}$ from multiple stations and synthetic model g(m)[R(f)]. w(i) is the weight for station i. $C_{\rm e}$ is a diagonal matrix of the square of uncertainties σ of the observational ratios at the corresponding frequency; we consider it

here to be uniform. The likelihood for the model m is as follows

$$\mathcal{L}(R_{\text{obs}}(f) \mid m) = \frac{1}{(\sqrt{2\pi C_{\text{e}}})^{l}} \exp\left(-\frac{\Phi(m)}{2}\right)$$
 (7)

where l denotes the data length. As before, we fix n=2 and $\gamma=2$ when searching for the minimum residuals (46). The full set of unknown model parameters is $m=\left[f_{c1},f_{c2},\frac{M_{01}}{M_{02}},\sigma\right]$. On the basis of the Bayesian posterior probability, the solution of the inversion is

$$\mathbb{P}\left(f_{c1}, f_{c2}, \frac{M_{01}}{M_{02}}, \sigma | R_{obs}(f)\right) = \frac{\mathcal{L}(R_{obs}(f) | m) \cdot \mathbb{P}\left(f_{c1}, f_{c2}, \frac{M_{01}}{M_{02}}, \sigma\right)}{\mathbb{I} \mathcal{L}(R_{obs}(f) | m) \cdot \mathbb{P}\left(f_{c1}, f_{c2}, \frac{M_{01}}{M_{02}}, \sigma\right) df_{c1} df_{c2} d\frac{M_{01}}{M_{02}} d\sigma}$$

We show in fig. S8 the 1D Gaussian probabilistic inversion for a regular earthquake of $M_{\rm j}=3.3$ at a depth of ~40 km in the orange column. The posterior probability of $f_{\rm c1}$ (blue bars), the corner frequency of the target earthquake, exhibits a rather unambiguous Gaussian distribution within 10 to 15 Hz. However, $f_{\rm c2}$, the averaged corner frequency of the empirical Green's function earthquakes is very likely outside of the studied frequency range of less than 30 Hz. The modeled ratio shown as the red star line matches well the global shape of the ratios from different seismic stations.

Seismic attenuation structure

To obtain a more detailed attenuation structure, we extend our spectral analysis to all events in the two columns. We start by using the f_c posterior of the probabilistic inversion above as an a priori to constrain site effects and minimize the ambiguities between source and site inherent to spectral inversion (47). We invert the displacement spectra $\Omega(f)$ for all the target events recorded at the same station and obtain relatively independent path-integrated attenuation t^* (48)

$$\Omega(f) = \frac{\Omega_0 e^{(-\eta f t^*)}}{\left[1 + (f/f_c)^{\gamma n}\right]^{1/\gamma}} \tag{9}$$

The full set of unknown model parameters can be described by $m = [\Omega_0, f_c, t^\star, \sigma]$. We interpret the average station residuals of the displacement spectra (at individual stations from all target earthquakes) that the fitted model cannot explain as the site effects that are unique to the station (14). We then correct the displacement spectra of all the earthquakes recorded using these site effects determined from the target events. To do this, we divide the displacement spectra of each event at each station by the averaged station residual. We then resolve for the source and path terms by modeling the corrected displacement spectra using Eq. 9.

As a quality control measure for the inversion of single displacement spectra, we select and retain t^* only when the corresponding σ , the uncertainty of data from probabilistic inversion, is below 0.2. From the definition $t^* = t/Q$, we solve the local seismic structure of quality factor Q over depth (Fig. 2, C and D) using the same least-squares inversion method as for the seismic velocity structure. The root mean square residuals for the attenuation inversion are reduced by 50 and 58% for the blue and orange columns, respectively. We compute the travel times using the previously inverted seismic velocity structure. As our purpose is to compare the relative depth variation within each of the two regions, as well as the relative relationship between Q_p and Q_s , we select the initial Q_0 for the

inversion by taking the minimum norm residual (fig. S9, C and D). Constant Q_0 values equal to 450 and 900 are separately set for the initial model in blue and orange columns, respectively. To avoid introducing any bias caused by using different prior values for the initial models, we set the Q_0 uniformly for P and S waves and jointly invert Q_D and Q_S for each depth column.

The inversion of 1D Q from regular earthquake spectra provides an average attenuation structure in each depth column. Despite inverting for the local 1D seismic velocities and attenuation, we note the lack of detailed structure at depths where there are few earthquakes. Earthquakes with a broad spatial distribution, especially in depth, are an indispensable prerequisite for obtaining robust estimates of the velocity and attenuation structure.

Empirical attenuation function

From Fig. 3 (A and B), we observe that the spectral energy of the low-frequency earthquakes decreases below the noise level above ~25 Hz. The low-frequency part of low-frequency earthquake spectra is comparable to the averaged low-frequency level of the spectra of regular earthquakes of slightly larger magnitude and is significantly higher than the low-frequency part of the noise. In comparison to the recorded frequency spectra of regular earthquakes, the fall-off rate of the low-frequency earthquake spectra is significantly greater at frequencies above 2 Hz.

We use an empirical attenuation function method to constrain the low-frequency earthquake source spectra using the attenuation measured from the probabilistic inversion for the regular earthquake displacement spectra. Each empirical attenuation function represents the difference between the best-fitting spectrum of a simple source model and the observed spectrum that incorporates path and site effects that cannot be simulated by simple exponential model of attenuation. We use these empirical attenuation functions to place constraints on the attenuation experienced by low-frequency events with similar paths occurring in the same depth column.

We show in fig. S10 an example empirical attenuation function in the blue column, where the blue curve represents the best model obtained from the probabilistic inversion, the red curve is the model without accounting for the exponential attenuation term $e^{(-\pi f f^*)}$ (Eq. 9), and the black curve is the observed spectrum. We then estimate the empirical attenuation as the difference between the red and black curves. We obtain 5 and 11 empirical attenuation functions from the local target earthquakes beneath station TOKH and TKWH, respectively, as shown in Fig. 3C. Both empirical attenuation functions and low-frequency earthquakes are averaged over the two horizontal components at station TKWH Fig. 3D. The flow-chart in fig. S11 provides a summary of the above steps used to obtain the empirical attenuation functions.

We correct the low-frequency earthquake spectra by removing the averaged empirical attenuation functions over three events closest to the depth range of low-frequency earthquakes. The spectra of both empirical attenuation functions and low-frequency earthquakes are averaged over the two horizontal components at station TKWH. The maximum frequency limit is set to 30 Hz considering the low signal-to-noise ratio at a higher frequency. We compare the low-frequency earthquakes' spectra before and after empirical attenuation function correction in Fig. 3D with the ω -square model (49) calculated using multiple theoretical f_c . This empirical attenuation function correction allows us to precisely capture

and evaluate the consequences of path effects on low-frequency earthquakes and investigate their source properties.

Source time functions of low-frequency earthquakes

The vast majority of low-frequency earthquakes is too small, with a sufficient signal-to-noise over too narrow a frequency range, to use the empirical Green's function approach to isolating the source from the path and site effects. That is why we adopted the methods described above. However, we can test our methods using the two largest low-frequency earthquakes with $M_{\rm j}=0.8$ and 0.9 for which we are able to find empirical Green's function events with a sufficient signal quality. We select two sets of smaller magnitude events to use as empirical Green's functions: low-frequency earthquakes and neighboring regular earthquakes. All the empirical Green's function events have a cross correlation of at least 0.7 (between 1 and 8 Hz) with the large low-frequency target events.

We select the regular earthquake empirical Green's functions from the events used in the inversion for velocity and attenuation structure; they have a magnitude of $M_i = 0.5$ and occur between depths of 35 and 45 km. Low-frequency earthquake empirical Green's functions are selected to have small magnitudes ($M_i \leq$ -0.2) with a low-frequency amplitude that is at least 10 times smaller than the target event. Figure S12 (A, C, and E) is the waveforms in different frequency bands of target low-frequency earthquakes and empirical Green's functions. There are five empirical Green's functions from regular earthquakes and five from low-frequency earthquakes. The time window enclosed by the vertical dashed lines is the time window used for the empirical Green's function deconvolution. We estimate the source-time functions of lowfrequency earthquakes using the same deconvolution procedure as for the regular earthquakes. The similarity of the source-time functions in Fig. 3 (C and E) supports our use of regular earthquakes for the retrieval of empirical attenuation functions and the source process of low-frequency earthquakes described above. We observe in fig. S12E that low-frequency earthquakes have a simple pulse source similar to regular earthquakes but with a duration significantly longer than even an earthquake of $M_i = 3.3$.

Stress drop

We estimate the stress drop ($\Delta\sigma$) of the target earthquakes from our corner frequency measurements and the calculated seismic moment (M_0) (50)

$$\Delta \sigma = \frac{7}{16} \frac{M_0}{d^3} \tag{10}$$

where *d* is source radius $d = k\beta/2\pi f_c$. *k* is a constant, and β is the shear-wave velocity in the vicinity zone of source.

A recent study (51) identified a significant discrepancy between the moment magnitudes and the JMA magnitudes M_j for small earthquakes, similar to the earthquakes we study here. Using the M_j to M_w relationship calculated by Uchide and Imanishi (51), we convert the local M_j into M_w and then calculate the seismic moment M_0 using the equation by Aki (49) $\log_{10}M_0 = 1.5M_w + 9.1$. We combine these values with our estimates of corner frequency to estimate stress drops. The stress drop from earthquakes in the two columns are similar and are consistent with typical global values (46). If we take an average corner frequency of a low-frequency earthquake as 2.5 Hz following Fig. 3D and assume that $M_j = 0.8$

 $\sim M_{\rm w}=$ 2, then we estimate a stress drop of about 10 kPa for a low-frequency earthquake.

We can also estimate the stress drop of low-frequency earth-quakes with past slip estimates of low-frequency earth-quakes. Recent work has estimated low-frequency earth-quakes to slip several microns during each event, along the San Andreas fault (18) and in the Cascadia subduction zone (52). If we assume that each low-frequency earth-quake slips (δ) 50 µm, then the expected slip velocity (δ) is 100 µm/s assuming an average source duration of (T) 0.5 s (1/ f_c). Assuming a circular rupture of area $A = \pi L^2$, where L is the radius, and combining the equations for seismic moment $M_0 = \mu \pi L^2 \delta$ and stress drop $\Delta \sigma = \mu \delta/2L$, where μ is the shear modulus, we can estimate the stress drop with

$$\Delta \sigma = \sqrt{\frac{\delta^3 \mu^3 \pi}{4M_0}} \tag{11}$$

For a low-frequency earthquake of $M_{\rm w}=1$, assuming $\mu=30$ GPa, we calculate a stress drop of ~8160 Pa. This estimate of ~8 kPa is similar to our other estimate of stress drop above, suggesting that low-frequency earthquake stress drops are about two orders of magnitude smaller than that of regular earthquakes (53).

Supplementary Materials

This PDF file includes: Figs. S1 to S13

REFERENCES AND NOTES

- J. R. Brown, G. C. Beroza, S. Ide, K. Ohta, D. R. Shelly, S. Y. Schwartz, W. Rabbel, M. Thorwart, H. Kao, Deep low-frequency earthquakes in tremor localize to the plate interface in multiple subduction zones. *Geophys. Res. Lett.* 36, L19306 (2009).
- W. B. Frank, B. Rousset, C. Lasserre, M. Campillo, Revealing the cluster of slow transients behind a large slow slip event. Sci. Adv. 4, eaat0661 (2018).
- 3. A. Kato, K. Obara, T. Igarashi, H. Tsuruoka, S. Nakagawa, N. Hirata, Propagation of slow slip leading up to the 2011 M(w) 9.0 Tohoku-Oki earthquake. *Science* **335**, 705–708 (2012).
- K. Obara, Connecting slow earthquakes to huge earthquakes. Science 353, 253–257 (2016).
- S. Ide, G. C. Beroza, D. R. Shelly, T. Uchide, A scaling law for slow earthquakes. Nature 447, 76–79 (2007).
- S. Ide, D. R. Shelly, G. C. Beroza, Mechanism of deep low frequency earthquakes: Further evidence that deep non-volcanic tremor is generated by shear slip on the plate interface. *Geophys. Res. Lett.* 34, L03308 (2007).
- R. Madariaga, High-frequency radiation from crack (stress drop) models of earthquake faulting. Geophys. J. Int. 51, 625–651 (1977).
- M. G. Bostock, A. M. Thomas, G. Savard, L. Chuang, A. M. Rubin, Magnitudes and momentduration scaling of low-frequency earthquakes beneath southern Vancouver Island. J. Geophys. Res. Solid Earth 120, 6329–6350 (2015).
- M. Matsubara, H. Sato, K. Uehira, M. Mochizuki, T. Kanazawa, Three-dimensional seismic velocity structure beneath Japanese islands and surroundings based on NIED seismic networks using both inland and offshore events. J. Disaster Res. 12, 844–857 (2017).
- Y. Yamamoto, S. Yada, K. Ariyoshi, T. Hori, N. Takahashi, Seismicity distribution in the Tonankai and Nankai seismogenic zones and its spatiotemporal relationship with interplate coupling and slow earthquakes. *Prog. Earth Planet. Sci.* 9, 32 (2022).
- S. Kita, M. Matsubara, Seismic attenuation structure associated with episodic tremor and slip zone beneath Shikoku and the Kii peninsula, southwestern Japan, in the Nankai subduction zone. J. Geophys. Res. Solid Earth 121, 1962–1982 (2016).
- N. Aso, K. Ohta, S. Ide, Tectonic, volcanic, and semi-volcanic deep low-frequency earthquakes in western Japan. *Tectonophysics* 600, 27–40 (2013).
- S. Kodaira, T. Iidaka, A. Kato, J. O. Park, T. Iwasaki, Y. Kaneda, High pore fluid pressure may cause silent slip in the Nankai trough. Science 304, 1295–1298 (2004).

SCIENCE ADVANCES | RESEARCH ARTICLE

- J. S. Nakai, A. F. Sheehan, R. E. Abercrombie, D. Eberhart-Phillips, Near trench 3D seismic attenuation offshore Northern Hikurangi Subduction Margin, North Island, New Zealand. Earth 126. e2020JB020810 (2021).
- M. G. Bostock, A. M. Thomas, A. M. Rubin, N. I. Christensen, On corner frequencies, attenuation, and low-frequency earthquakes. J. Geophys. Res. Solid Earth 122, 543–557 (2017).
- D. Eberhart-Phillips, S. Bannister, M. Reyners, Deciphering the 3-D distribution of fluid along the shallow Hikurangi subduction zone using P- and S-wave attenuation. *Geophys. J. Int.* 211, 1032–1045 (2017).
- J. Mori, A. Frankel, Source parameters for small events associated with the 1986 North Palm Springs, California, earthquake determined using empirical Green functions. *Bull. Seismol. Soc. Am.* 80, 278–295 (1990).
- A. M. Thomas, G. C. Beroza, D. R. Shelly, Constraints on the source parameters of lowfrequency earthquakes on the San Andreas Fault. Geophys. Res. Lett. 43, 1464–1471 (2016).
- A. Katsumata, N. Kamaya, Low-frequency continuous tremor around the moho discontinuity away from volcanoes in the Southwest Japan. Geophys. Res. Lett. 30, 1020 (2003).
- K. Obara, K. Kasahara, S. Hori, Y. Okada, A densely distributed high-sensitivity seismograph network in Japan:Hi-net by National Research Institute for Earth Science and Disaster Prevention. Rev. Sci. Instrum. 76, 021301 (2005).
- K. Ohta, K. Shiomi, T. Matsuzawa, Complex interaction, striations, and periodicity of deep tremor surrounding a tremor gap in the central nankai subduction zone, Japan. J. Geophys. Res. Solid Earth 128. e2022JB025373 (2023).
- W. B. Frank, N. M. Shapiro, A. L. Husker, V. Kostoglodov, A. Romanenko, M. Campillo, Using systematically characterized low-frequency earthquakes as a fault probe in Guerrero, Mexico. J. Geophys. Res. Solid Earth 119, 7686–7700 (2014).
- D. R. Shelly, G. C. Beroza, S. Ide, S. Nakamula, Low-frequency earthquakes in Shikoku, Japan, and their relationship to episodic tremor and slip. *Nature* 442. 188–191 (2006).
- W. B. Frank, N. M. Shapiro, V. Kostoglodov, A. L. Husker, M. Campillo, J. S. Payero, G. A. Prieto, Low-frequency earthquakes in the mexican sweet spot. *Geophys. Res. Lett.* 40, 2661–2666 (2013).
- D. T. Trugman, P. M. Shearer, GrowClust: A hierarchical clustering algorithm for relative earthquake relocation, with application to the Spanish Springs and Sheldon, Nevada, earthquake sequences. Seismol. Res Lett. 88, 379–391 (2017).
- J. Nakajima, A. Hasegawa, Tremor activity inhibited by well-drained conditions above a megathrust. Nat. Commun. 7, 13863 (2016).
- Q.-Y. Wang, M. Campillo, F. Brenguier, A. Lecointre, T. Takeda, K. Yoshida, Seismic evidence
 of fluid migration in northeastern Japan after the 2011 tohoku-oki earthquake. *Earth Planet. Sci. Lett.* 563, 116894 (2021).
- 28. E. Kissling, Velest user's guide. Int. Inst. Geophys., 1–26 (1995).
- A. F. Arnulf, D. Bassett, A. J. Harding, S. Kodaira, A. Nakanishi, G. Moore, Upper-plate controls on subduction zone geometry, hydration and earthquake behaviour. *Nat. Geosci.* 15, 143–148 (2022).
- K. W. Winkler, A. Nur, Seismic attenuation: Effects of pore fluids and frictional sliding. Geophysics 47, 1–15 (1982).
- A. Kato, T. Iidaka, R. Ikuta, Y. Yoshida, K. Katsumata, T. Iwasaki, S. Sakai, C. Thurber, N. Tsumura, K. Yamaoka, T. Watanabe, T. Kunitomo, F. Yamazaki, M. Okubo, S. Suzuki, N. Hirata, Variations of fluid pressure within the subducting oceanic crust and slow earthquakes.
 Geophys. Res. Lett. 37. L14310 (2010).
- A. Kato, A. Saiga, T. Takeda, T. Iwasaki, T. Matsuzawa, Non-volcanic seismic swarm and fluid transportation driven by subduction of the Philippine Sea slab beneath the Kii Peninsula, Japan. *Planets Space* 66, 86 (2014).
- 33. B. L. N. Kennett, E. R. Engdahl, R. Buland, Constraints on seismic velocities in the Earth from travel times. *Geophys. J. Int.* **122**, 108–124 (1995).
- S. Yabe, A. S. Baltay, S. Ide, G. C. Beroza, Seismic-wave attenuation determined from tectonic tremor in multiple subduction zones. Bull. Seismol. Soc. Am. 104, 2043–2059 (2014).
- G. Farge, N. M. Shapiro, W. B. Frank, Moment-duration scaling of low-frequency earthquakes in Guerrero, Mexico. J. Geophys. Res. Solid Earh 125, e2019JB019099 (2020).
- C. Fliedner, M. E. French, Measurements of wave-induced attenuation in saturated metapelite and the band-limitation of low-frequency earthquakes. AGU Adv. 4, e2022AV000837 (2023).

- M. Gori, V. Rubino, A. J. Rosakis, N. Lapusta, Dynamic rupture initiation and propagation in a fluid-injection laboratory setup with diagnostics across multiple temporal scales. *Proc. Natl. Acad. Sci. U.S.A.* 118, e2023433118 (2021).
- P. Segall, A. M. Rubin, A. M. Bradley, J. R. Rice, Dilatant strengthening as a mechanism for slow slip events. J. Geophys. Res. Solid Earth 115, B12305 (2010).
- Q.-Y. Wang, B. W. Frank, E. R. Abercrombie, What makes low-frequency earthquakes low frequency: Cluster-based constraints on the attenuation structure of the Nankai plate interface (Japan). AGU Fall Meeting Abstracts 2021, S21B (2021).
- K. Tamaribuchi, Evaluation of automatic hypocenter determination in the JMA unified catalog. Earth Planets Space 70, 141 (2018).
- F. J. Hilterman, Interpretative lessons from three-dimensional modeling. Geophysics 47, 784–808 (1982).
- R. E. Abercrombie, Stress drops of repeating earthquakes on the San Andreas Fault at Parkfield. Geophys. Res. Lett. 41, 8784–8791 (2014).
- G. A. Prieto, M. Denolle, J. F. Lawrence, G. C. Beroza, On amplitude information carried by the ambient seismic field. *Comptes Rendus – Geosci.* 343, 600–614
- R. E. Abercrombie, P. Leary, Source parameters of small earthquakes recorded at 2.5 km depth, Cajon pass, southern California: Implications for earthquake scaling. *Geophys. Res. Lett.* 20, 1511–1514 (1993).
- C. Van Houtte, M. Denolle, Improved model fitting for the empirical Green's function approach using hierarchical models. J. Geophys. Res. Solid Earth 123, 2923–2942 (2018).
- B. P. Allmann, P. M. Shearer, Global variations of stress drop for moderate to large earthquakes. J. Geophys. Res. 114, B01310 (2009).
- P. M. Shearer, R. E. Abercrombie, D. T. Trugman, W. Wang, Comparing egf methods for estimating corner frequency and stress drop from P wave spectra. J. Geophys. Res. Solid Earth 124, 3966–3986 (2019).
- F. Scherbaum, Combined inversion for the three-dimensional Q structure and source parameters using microearthquake spectra. J. Geophys. Res. Solid Earth 95, 12423 (1990).
- 49. K. Aki, Scaling law of seismic spectrum. J. Geophys. Res. 72, 1217–1231 (1967).
- J. D. Eshelby, The determination of the elastic field of an ellipsoidal inclusion, and related problems. Proc. Math. Phys. Sci. 241, 376–396 (1957).
- T. Uchide, K. Imanishi, Underestimation of microearthquake size by the magnitude scale of the Japan Meteorological Agency: Influence on earthquake statistics. J. Geophys. Res. Solid Earth 123, 606–620 (2018).
- S. Chestler, K. Creager, Evidence for a scale-limited low-frequency earthquake source process. J. Geophys. Res. Solid Earth 122, 3099–3114 (2017).
- E. E. Brodsky, J. Mori, Creep events slip less than ordinary earthquakes. Geophys. Res. Lett. 34, 16309 (2007).
- F. Hirose, J. Nakajima, A. Hasegawa, Three-dimensional seismic velocity structure and configuration of the Philippine Sea slab in southwestern Japan estimated by double-difference tomography. J. Geophys. Res. Solid Earth 113, B09315 (2008).

Acknowledgments

Funding: W.B.F and R.E.A acknowledge support from the National Science Foundation under EAR award #2103408. Author contributions: Conceptualization: All authors. Methodology: Q.-Y.W., W.B.F., and R.E.A. Visualization: Q.-Y.W. Funding acquisition: W.B.F. and R.E.A. Writing—original draft: Q.-Y.W., W.B.F., and R.E.A. Writing—review and editing: All authors. Competing interests: The authors declare that they have no competing interests. Data and materials availability: All data needed to evaluate the conclusions in the paper are present in the paper and/or the Supplementary Materials. Hi-net seismic data required in the paper are available from the National Research Institute for Earth Science and Disaster Prevention (NIED; www. hinet.bosai.go.jp). The earthquake catalogs used in the paper are available from the JMA (www. data.jma.go.jp/svd/eqev/data/bulletin/catalog/notes_e.html).

Submitted 27 February 2023 Accepted 7 July 2023 Published 9 August 2023 10.1126/sciady.adh3688